Supporting Information

Highly dispersed platinum on honeycomb-like NiO@Ni film as a synergistic electrocatalyst for hydrogen evolution reaction

Zheng-Jun Chen,[†,§] Guo-Xuan Cao,[†,§] Li-Yong Gan,*[,†] Hao Dai,[†] Ning Xu,[†] Ming-Jie Zang,[†] Hong-Bin Dai,[†] Hui Wu,[‡] and Ping Wang*[,†]

[†] School of Materials Science and Engineering, Key Laboratory of Advanced Energy Storage Materials of Guangdong Province, South China University of Technology, Guangzhou 510641, People's Republic of China

[‡] NIST Center for Neutron Research, National Institute of Standards and Technology, Gaithersburg, Maryland 20899-6102, United States

E-mail for L. Y. Gan: ganly@scut.edu.cn, E-mail for P. Wang: mspwang@scut.edu.cn

Experimental Section

***Theoretical Calculations*:** Density functional theory calculations were performed using the Vienna Ab-Initio Simulation Package with spin-polarized Perdew-Burke-Ernzerhof exchange correlation functional including van der Waals corrections (optB88).[1–3] A cutoff energy of 500 eV was used for the plane-wave expansion.[4,5] A 3×3 lateral supercell and a four-layer slab were used to model Pt (111) surface. NiO/Pt interface was described by an inverse model,[6,7] in which a (3×3) NiO (100) ribbon was deposited on a three-layer ($5\sqrt{3}\times3$) Pt (111) slab. An effective U of 5.3 eV for Ni was used to describe on-site Coulomb interaction in the localized 3d orbitals and magnetic interaction (antiferromagnetic) in NiO.[8] In each case, a vacuum thickness of at least 20 Å was applied to prevent unphysical interaction between periodic images. The adsorbed species and the top two layers of Pt (111) and NiO/Pt were fully relaxed until all residual forces were less than 0.02 eV/Å, while the remaining layers were fixed. The Brillouin zone was sampled by a (3×3×1) and (1×3×1) Gamma-centered **k**-mesh for Pt (111) and NiO/Pt, respectively. The reaction barriers of water dissociation were determined by climbing-image nudged elastic band method.[9] The adsorption energy (ΔE) of H was defined as

$$\Delta E = E_{\mathrm{H/surface}} - 1/2E_{\mathrm{H2}} - E_{\mathrm{surface}} \qquad (1)$$

where $E_{\mathrm{H/surface}}$, E_{H2} and E_{surface} are the total energies of H adsorbed surfaces, H_2 in gas phase and clean surfaces, respectively. The associated change of Gibbs free energy of H was calculated as

$$\Delta G = \Delta E + \Delta ZPE - T\Delta S \qquad (2)$$

with ΔZPE and ΔS being the differences of zero-point energy and of entropy between the adsorbed state and gas phase. The *ZPE* and entropies were calculated from the vibrational frequencies.[10,11]

***Chemicals and Materials*:** The nickel foam (NF, ≥ 99%) with a thickness of 1.7 mm, an area density of about 480 $g \cdot m^{-2}$ and an average pore size of 0.3 mm was purchased from Incoatm. hydrochloric acid (HCl, 36~38 wt%), potassium hydroxide (KOH, 95%), nickel sulfate hexahydrate ($NiSO_4 \cdot 6H_2O$, 98.5%), copper sulfate hexahydrate ($CuSO_4 \cdot 6H_2O$, 99.5%), boric acid (H_3BO_3, 99%), chloroplatinic acid hexahydrate ($H_2PtCl_6 \cdot 6H_2O$, Pt ≥ 37.5%), Pt/C (20 wt% Pt on Vulcan XC-72R), nafion solution (5 wt% in mixture of lower aliphatic alcohols and water) and other reagents of analytical grade were all obtained from commercial sources and used as received. Deionized (DI) water was used throughout the experiments.

***Synthesis of NiO@Ni/NF Sample*:** The NiO@Ni/NF sample was prepared by the previous reported method with slight modification.[12,13] A Ni/Cu film was first deposited on NF by a electrodeposition method in a three-electrode cell using the NF (1 cm × 2 cm) as the working electrode, a nickle plate counter electrode and a saturated calomel electrode (SCE) reference electrode. The electroplating solution consisted of 1 M $NiSO_4 \cdot 6H_2O$, 0.5 M H_3BO_3 and 0.01 M $CuSO_4 \cdot 6H_2O$. Prior to deposition, NF was ultrasonically cleaned in ethanol for 10 min, followed by immersing in a 3.0 M HCl solution for 10 min and washing with DI water. The electroplation was carried out at a constant potential of –0.85 V vs. SCE for 20 min. Subsequently, selective dissolution of Cu from the Ni/Cu film was conducted in the same solution by applying an anodic potential of 0.2 V vs. SCE for 15 min. According to the weight change of the sample before and after electroplation and electrochemical etching, the loading amount of NiO@Ni

layer on the NF was determined to be ~2.0 mg·cm^{-2}.

***Synthesis of Pt/NiO@Ni/NF Electrocatalyst*:** The as-prepared NiO@Ni/NF sample was immersed in 2 mL of 0.58 mM $H_2PtCl_6 \cdot 6H_2O$ solution for 4 h, followed by thorough washing by the mixture of DI water and acetone. Thus-prepared sample was finally subjected to an electrochemical reduction process that was conducted at a potential of −0.04 V vs. the reversible hydrogen electrode (RHE) for 10 minutes in a three-electrode cell. The Pt content of the targeted catalyst was measured by inductively coupled plasma-atomic emission spectrometry (ICP-AES) technique. More exactly, the concentrations of $[PtCl_6]^{2-}$ before and after the electrostatic adsorption process were measured by ICP-AES, the difference of which gave the loading amount of Pt on the targeted catalyst.

***Synthesis of Pt@Ni/NF Electrocatalyst*:** The as-prepared NiO@Ni/NF sample was first treated by 3 M hydrochloric acid (HCl) solution for 0.5 h to remove the NiO passivation film. After being washed thoroughly with DI water, the sample was then immersed in 2 mL of 0.58 mM $H_2PtCl_6 \cdot 6H_2O$ solution for 4 h. According to the concentration change of $[PtCl_6]^{2-}$ before and after the galvanic replacement process, as measured by ICP-AES, the Pt content of the Pt@Ni/NF catalyst was determined to be ~0.113 mg·cm^{-2}.

***Preparation of the Pt/C Electrode*:** In preparation of the Pt/C electrode, 5 mg of Pt/C catalyst was first dispersed in 1 mL isopropanol and 50 μL of 5 wt% Nafion solution was then added as the binding agent. The mixture was sonicated for at least 30 min, and 20 μL of the resulting catalyst ink was drop-casted on a glass carbon electrode with a geometric area of 0.07 cm^2.

***Characterization*:** The phase structure of the catalyst samples was analyzed by an X-ray diffractometer (Rigaku RINT 2000) with Cu Kα radiation. The morphology and microstructure of the catalyst samples were studied using field-emission scanning electron microscope (FE-SEM, ZEISS MERLIN) and high-resolution transmission electron microscopy (HRTEM, JEOL-2100F), both equipped with an energy dispersive X-Ray spectroscopy analysis unit (Oxford). The chemical states of the constituent elements of the catalyst samples were analyzed by X-ray photoelectron spectroscopy (XPS, Thermo Scientific ESCALAB 250 xi) with Al Kα X-ray source. In the XPS measurements, high-resolution scans of elemental lines were recorded at 50 eV pass energy of the analyzer. All the binding energies (BEs) were calibrated using the C 1s peak (at 284.8 eV) of the adventitious carbon as an internal standard. The curve fitting was performed using XPS PEAK 4.1 software. In the XPS depth profile analysis, the Ar^+ ion beam energy was adjusted to 2000 eV. The ion beam current density was around 1.0 μA·mm^{-2}. Under the applied etching conditions, the etch rate was estimated to be around 0.11 nm·s^{-1}. Raman spectra were collected using a Thermo Fisher Micro DXR microscope with a He-Ne laser (532 nm) excitation source at a resolution of 2 cm^{-1}. Before the measurement session, the instrument calibration was performed using the alignment/calibration tool supplied by the manufacturer. Temperature-programmed reduction (TPR) measurements were carried out on a Micromeritics AutoChem II 2920 automated catalyst characterization system. The Pt content of the catalyst samples was measured by inductively coupled plasma-atomic emission spectrometry (ICP-AES, Iris Intrepid) technique.

***Electrochemical Measurements*:** Electrochemical measurements were conducted in a three-electrode setup using a CHI 660E electrochemical analyzer. The electrochemical cell consists of a catalytic electrode as the working electrode, a graphite plate counter electrode and a Hg/HgO (with 1 M KOH) reference electrode. The electrochemical performance of the catalysts was investigated in 1 M KOH solution. Polarization curves were measured at a sweep rate of 2 $mV \cdot s^{-1}$ without iR compensation in a range of +0.02~−0.45 V vs. RHE. Potentials, measured versus Hg/HgO, were referenced to RHE by adding a value of (0.098 + 0.059×pH) V. The electrochemical impedance spectroscopy (EIS) measurements were performed using above three-electrode system at −1.0 V vs. Hg/HgO. The impedance spectra were collected in a frequency range of 100 kHz~0.1 Hz with a 5 mV amplitude.

***Determination of Faradaic Efficiency (FE)*:** The amount of generated O_2 and H_2 during overall water splitting process was measured using a classic water drainage method. The FE was calculated by comparing the experimentally measured gas amount with theoretically calculated value.

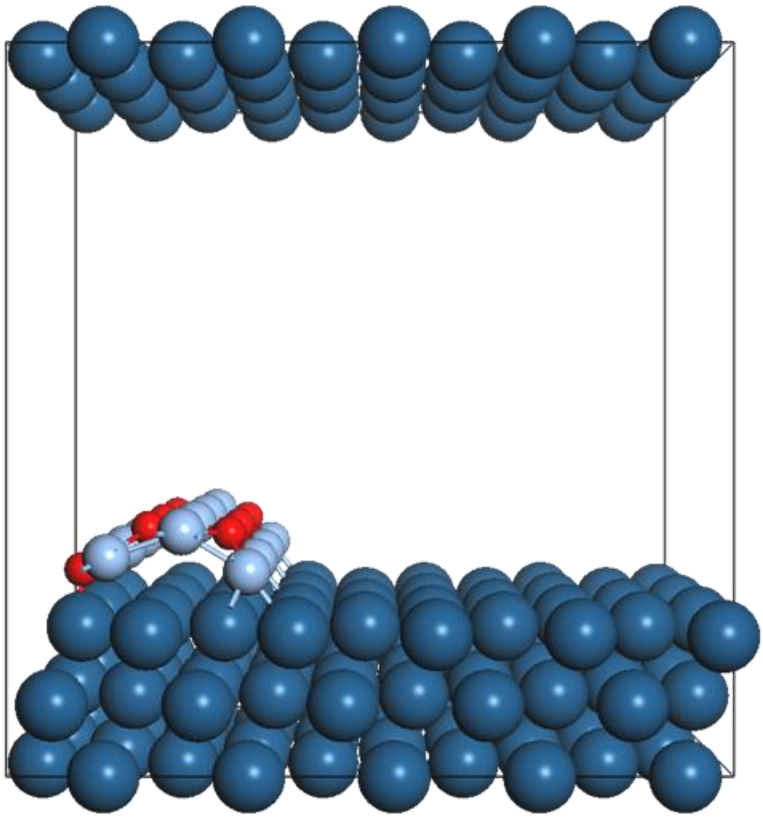

Figure S1. Structural model of NiO/Pt interface. The large dark blue, small light blue, and red balls represent Pt, Ni, and O atoms, respectively.

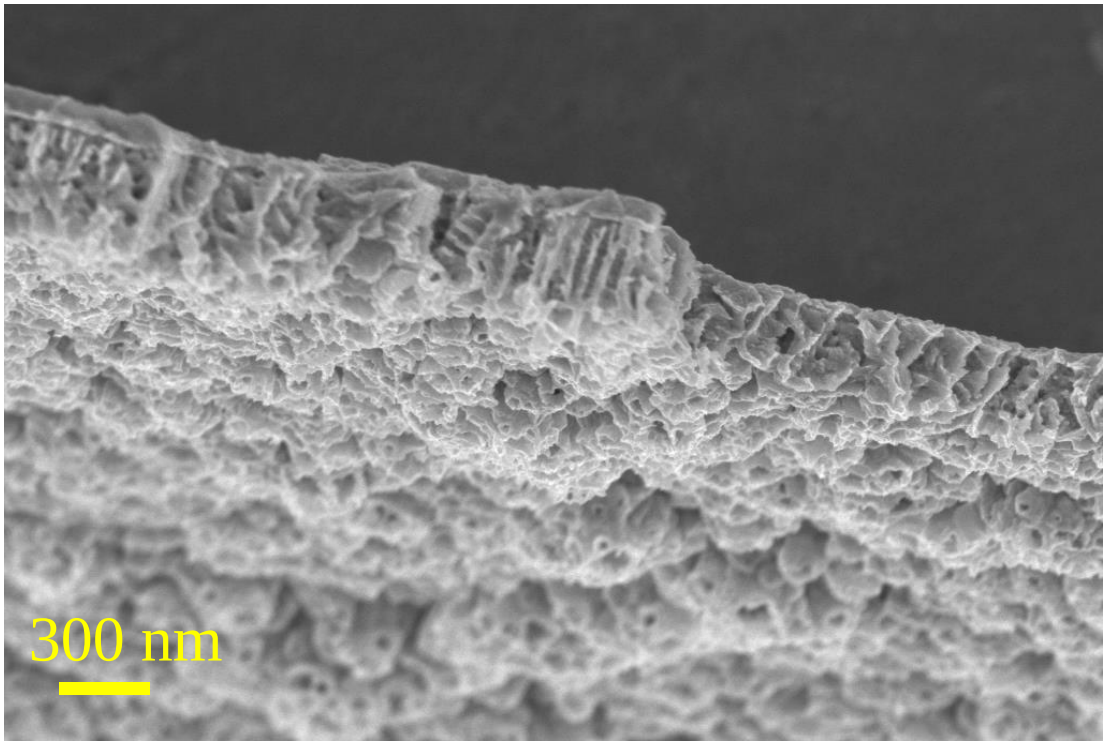

Figure S2. The FE-SEM of the NiO@Ni/NF sample.

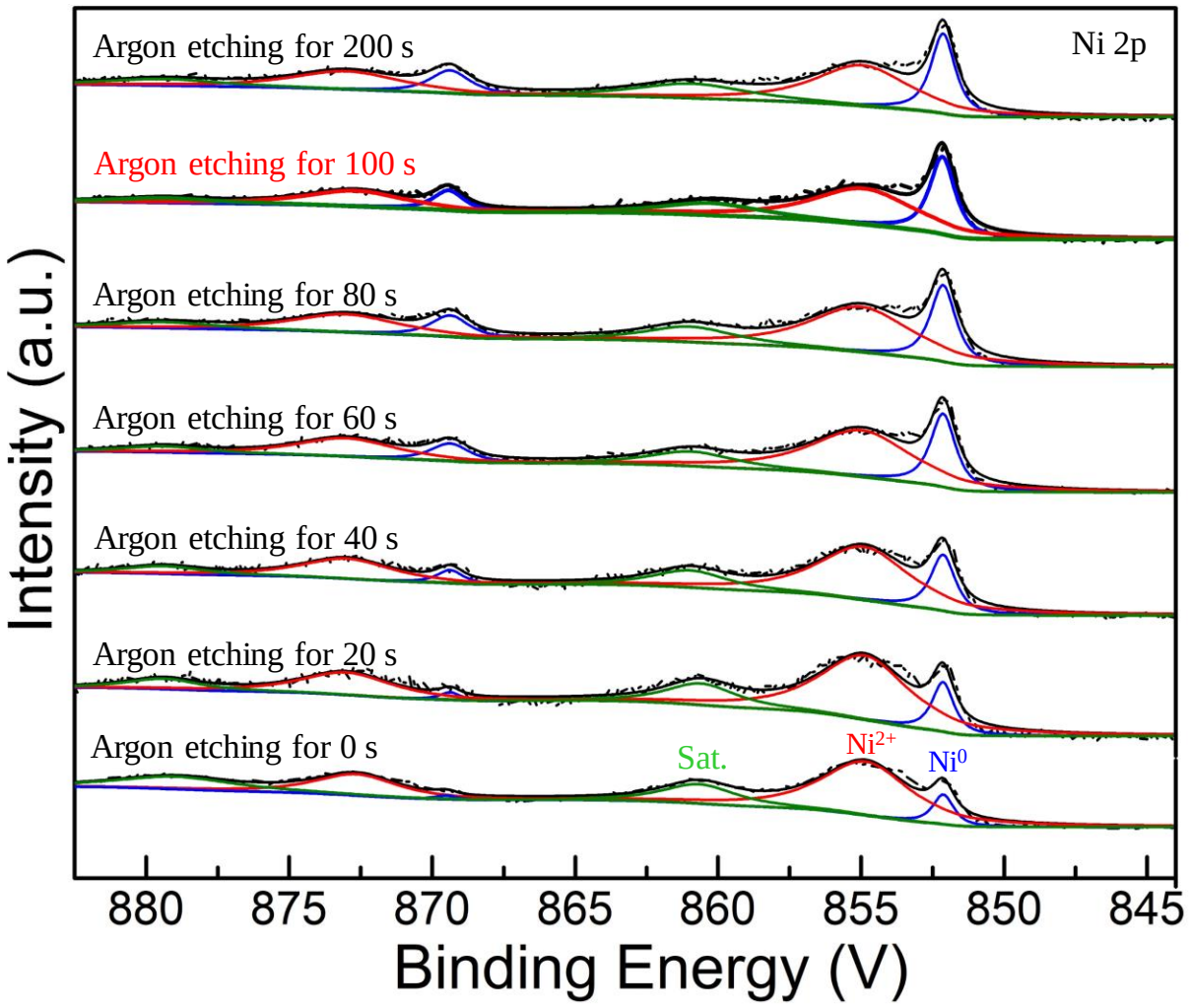

Figure S3. XPS spectra of Ni 2p region of the NiO@Ni/NF sample etched by Ar^+ for 0−200 s.

The etching rate was calculated following the Equation[14]: Etching rate=10^{-2}·$IYw/(\rho A)$ nm·s^{-1}, where I is the ion beam current in μA, Y is sputter yield, w is atomic weight, ρ is density and A is the sputter area in mm^2. Based on the published sputter yield data and the applied experimental parameters, the etching rate upon Ar^+ sputtering was calculated to be around 0.11 nm·s^{-1}. The XPS depth profile analysis showed that the signal intensities of Ni^{2+} and Ni^0 became largely stable after Ar^+ etching for 100 s. According to these measured and calculated results, the thickness of NiO film was estimated to be around 11 nm.

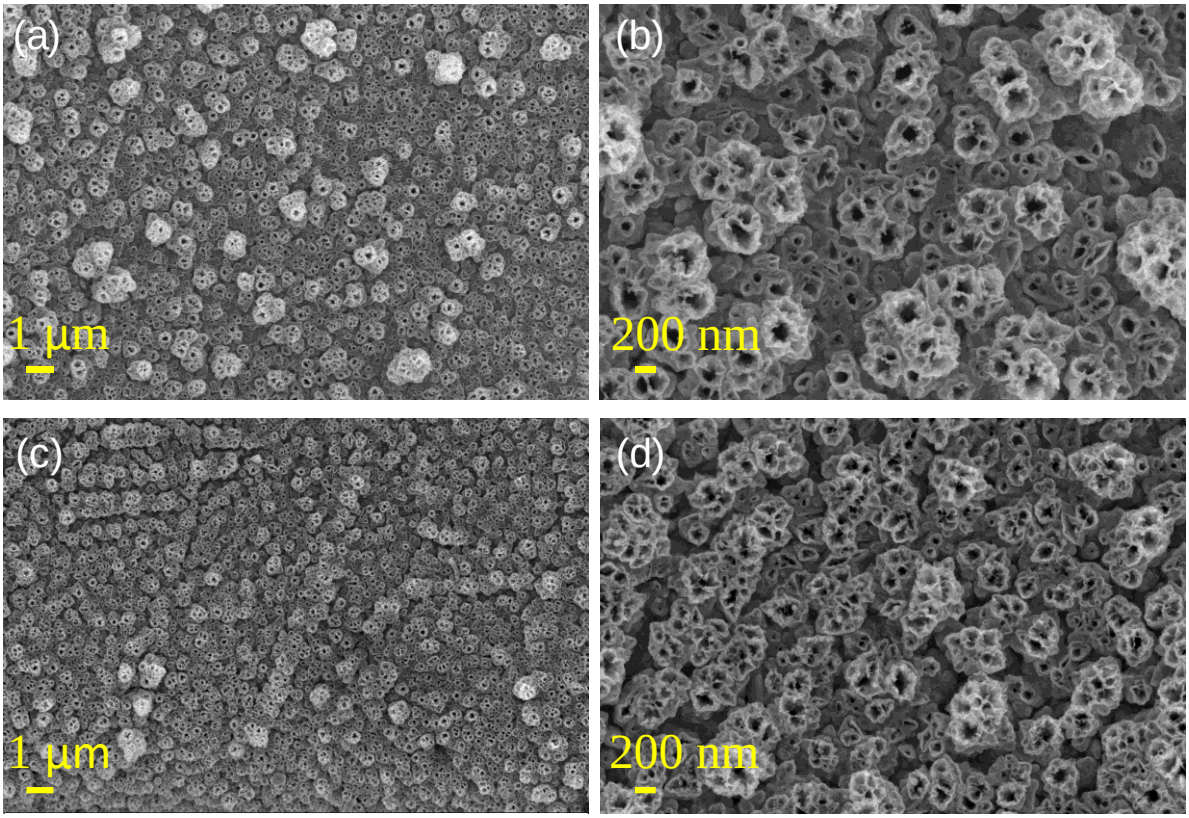

Figure S4. FE-SEM images at different magnifications of the as-prepared Pt/NiO@Ni/NF catalyst (a, b) and those after 24 h durability test (c, d).

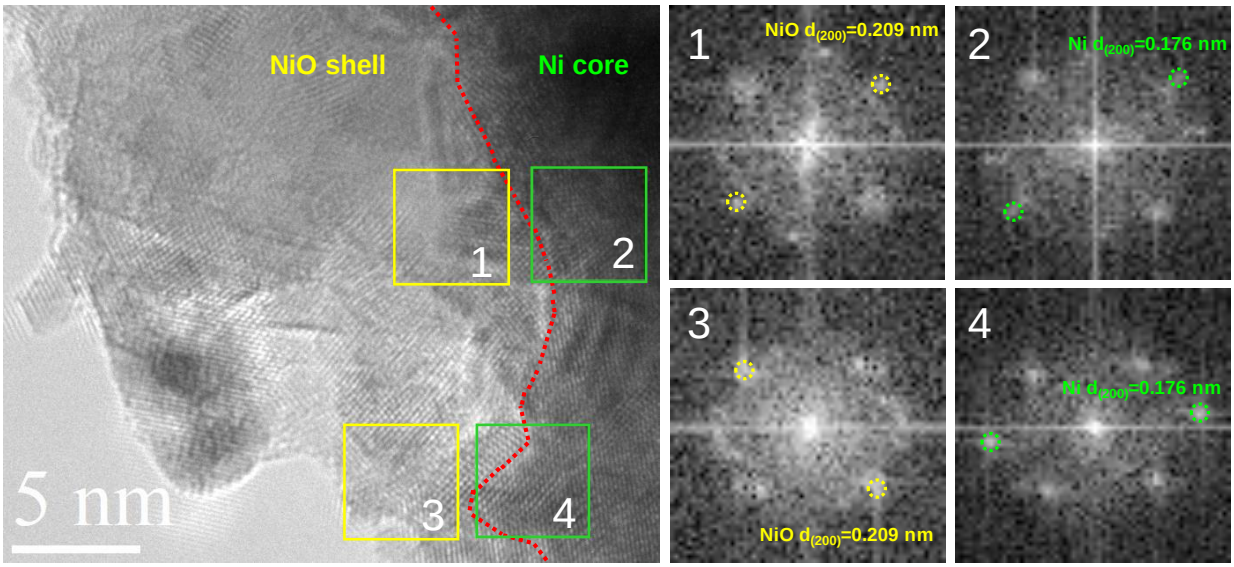

Figure S5. The HRTEM image of Pt/NiO@Ni/NF and the corresponding fast Fourier transform (FFT) images of the selected regions 1, 2, 3, and 4.

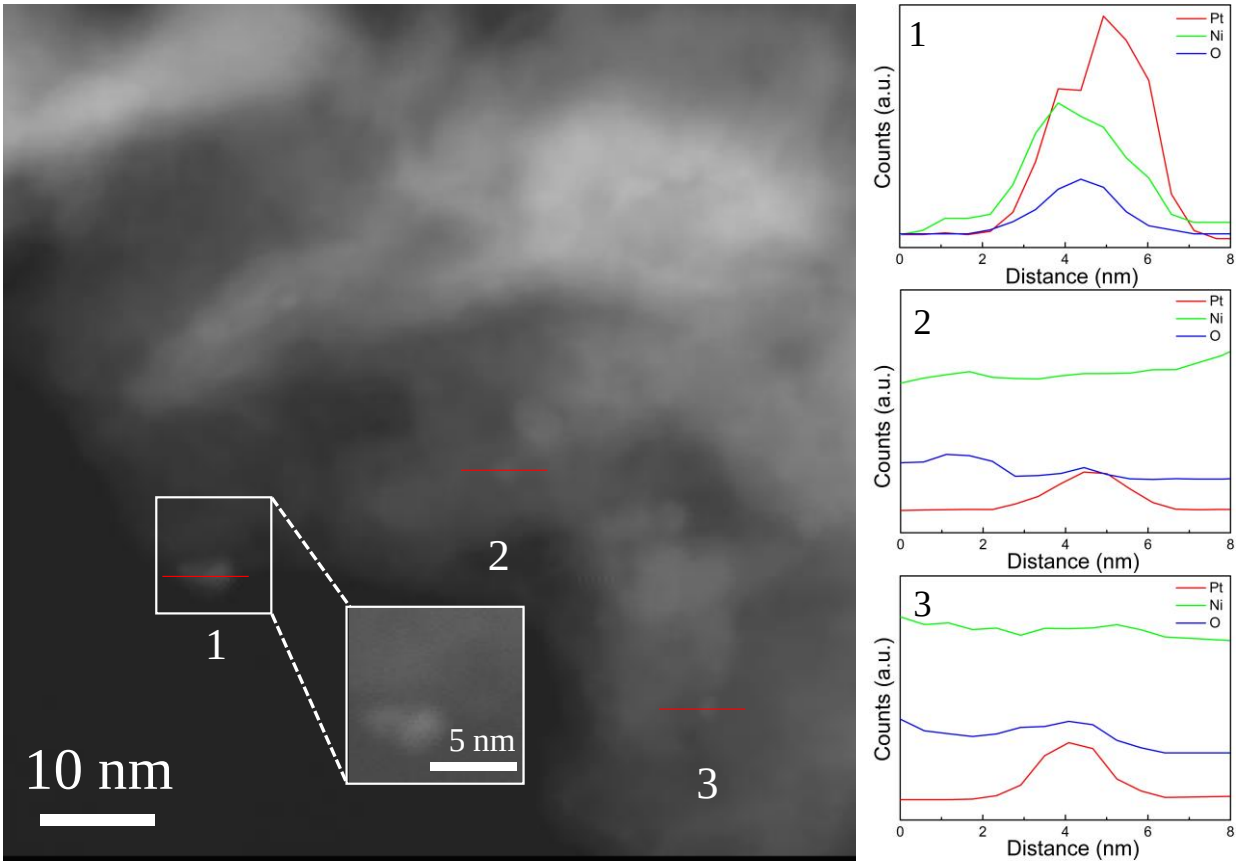

Figure S6. The HAADF-STEM image of Pt/NiO@Ni/NF, and the EDX line-scanning profiles along the direction indicated by the red line. The inset show high magnification STEM image.

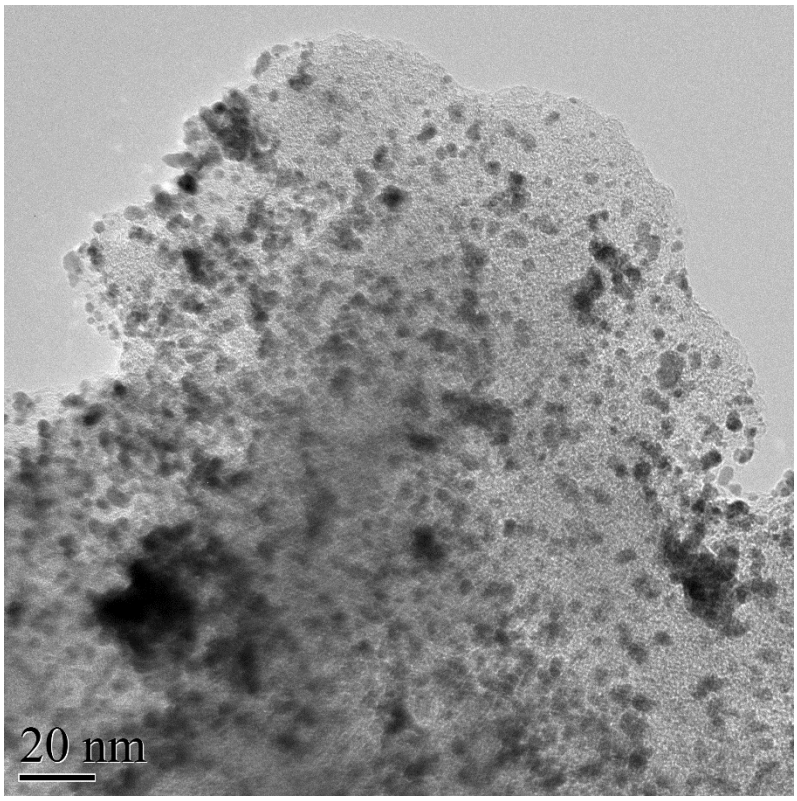

Figure S7. The TEM image of Pt/C catalyst.

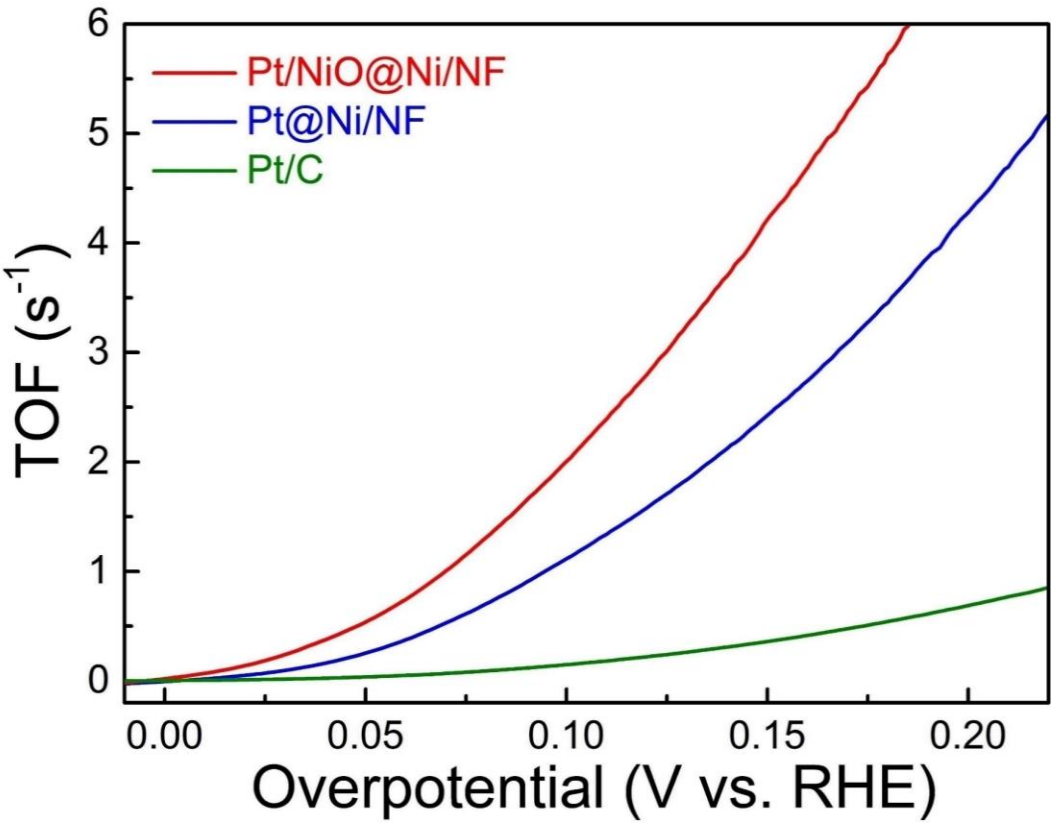

Figure S8. The turnover frequency (TOF) value of Pt/NiO@Ni/NF, Pt@Ni/NF, and Pt/C catalysts at different overpotentials.

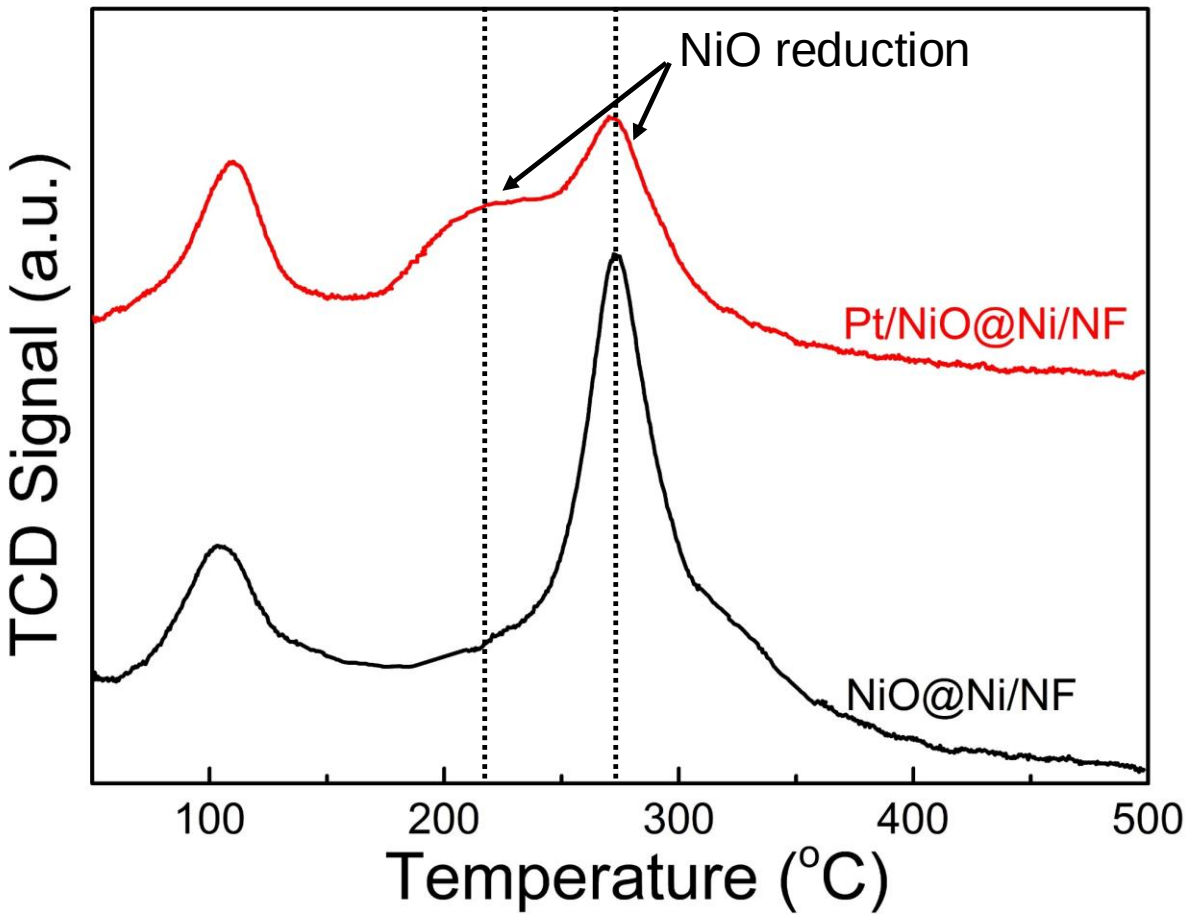

Figure S9. The TPR profiles (upward peaks indicate H_2 consumption) of Pt/NiO@Ni/NF and NiO@Ni/NF samples.

Table S1. A comparison of the HER activities of various electrocatalysts.

Electrocatalyst	Overpotential (mV) (η@10 mA·cm^{-2})	Tafel slope (mV·dec^{-1})	Electrolyte	Reference
Pt/NiO@Ni/NF	34	40	1 M KOH	This work
$Ni(OH)_2/MoS_2$	80	60	1 M KOH	[11]
FeS_2	96	78	1 M KOH	[15]
CoMoP@C	81	55.53	1 M KOH	[16]
Mo_2C@2D-NPCs	~45	46	1 M KOH	[17]
N-doped Mo_2C	110	49.7	1 M KOH	[18]
Ni–Mo nitride	89	79	1 M KOH	[19]
$Ni_{0.33}Co_{0.67}Se_2$	106	60	1 M KOH	[20]
FeB_2	61	87.5	1 M KOH	[21]
Pt NWs/SL-$Ni(OH)_2$	70 mV at 2.48 mA·cm^{-2}	/	1 M KOH	[22]
PtCoFe@CN	45	36	0.5 M H_2SO_4	[23]
ALD 50 Pt/NGNs	40	29	0.5 M H_2SO_4	[24]
Pd/Cu-Pt NRs	22.8	25	0.5 M H_2SO_4	[25]
Pt@PCM	105	65.3	0.5 M H_2SO_4	[26]
PtSA-NT-NF	24	30	Phosphate buffer (pH 7.2)	[27]

Supporting References

(1) Perdew, J. P.; Burke, K.; Ernzerhof, M. Generalized Gradient Approximation Made Simple. *Phys*. *Rev*. *Lett*. **1996**, *77*, 3865−3868.

(2) Klimeš, J.; Bowler, D. R.; Michaelides, A. A Critical Assessment of Theoretical Methods for Finding Reaction Pathways and Transition States of Surface Processes. *J. Phys.: Condens. Matter* **2010**, *22*, 074203.

(3) Klimeš, J.; Bowler, D. R.; Michaelides, A. Van der Waals Density Functionals Applied to Solids. *Phys*. *Rev*. *B* **2011**, *83*, 195131.

(4) Blöchl, P. E.; Projected Augmented-Wave Method. *Phys. Rev. B* **1994**, *50*, 17953−17979.

(5) Kresse, G.; Joubert, D. From Ultrasoft Pseudopotentials to the Projector Augmented-Wave Method. *Phys. Rev. B* **1999**, *59*, 1758.

(6) Fu, Q.; Li, W. X.; Yao, Y.; Liu, H.; Su, H. Y.; Ma, D.; Gu, X. K.; Chen, L.; Wang, Z.; Zhang, H.; Wang, B.; Bao, X. Interface-Confined Ferrous Centers for Catalytic Oxidation. *Science* **2010**, *328*, 1141−1144.

(7) Gao, D.; Zhang, Y.; Zhou, Z.; Cai, F.; Zhao, X.; Huang, W.; Li, Y.; Zhu, J.; Liu, P.; Yang, F.; Wang, G.; Bao, X. Enhancing CO_2 Electroreduction with the Metal-Oxide Interface. *J. Am. Chem. Soc*. **2017**, *139*, 5652−5655.

(8) Staroverov, V. N.; Scuseria, G. E.; Tao, J.; Perdew, J. P. Tests of a Ladder of Density Functionals for Bulk Solids and Surfaces. *Phys. Rev. B* **2004**, *69*, 075102.

(9) Henkelman, G.; Uberuaga, B. P.; Jónsson, H. A Climbing Image Nudged Elastic Band Method for Finding Saddle Points and Minimum Energy Paths. *J. Chem. Phys.* **2000**, *113*, 9901−9904.

(10) Nørskov, J. K.; Rossmeisl, J.; Logadottir, A.; Lindqvist, L. Origin of the Overpotential for Oxygen Reduction at a Fuel-Cell Cathode. *J. Chem. Phys. B* **2004**, *108*, 17886−17892.

(11) Zhang, B.; Liu, J.; Wang, J.; Ruan, Y.; Ji, X.; Xu, K.; Chen, C.; Wan, H.; Miao, L.; Jiang, J. Interface Engineering: The $Ni(OH)_2/MoS_2$ Heterostructure for Highly Efficient Alkaline Hydrogen Evolution. *Nano Energy* **2017**, *37*, 74−80.

(12) Sun, L.; Chien, C. L.; Searson, P. C. Fabrication of Nanoporous Nickel by Electrochemical Dealloying. *Chem. Mater.* **2004**, *16*, 3125−3129.

(13) Dai, X.; Chen, D.; Fan, H.; Zhong, Y.; Chang, L.; Shao, H.; Wang, J.; Zhang, J.; Cao, C. N. $Ni(OH)_2$/NiO/Ni Composite Nanotube Arrays for High-Performance Supercapacitors. *Electrochim. Acta* **2015**, *154*, 128−135.

(14) Watts, J. F.; Wolstenholme, J. An Introduction to Surface Analysis by XPS and AES; Wiley: Chichester, U.K., 2003, 93−106.

(15) Miao, R.; Dutta, B.; Sahoo, S.; He, J.; Zhong, W.; Cetegen, S. A.; Jiang, T.; Alpay, S. P.; Suib, S. L. Mesoporous Iron Sulfide for Highly Efficient Electrocatalytic Hydrogen Evolution. *J. Am. Chem. Soc.* **2017**, *139*, 13604−13607.

(16) Ma, Y. Y.; Wu, C. X.; Feng, X. J.; Tan, H. Q.; Yan, L. K.; Liu, Y.; Kang, Z. H.; Wang, E. B.; Li, Y. G. Highly Efficient Hydrogen Evolution from Seawater by a Low-Cost and Stable CoMoP@C Electrocatalyst Superior to Pt/C. *Energy Environ. Sci.* **2017**, *10*, 788−798.

(17) Lu, C.; Tranca, D.; Zhang, J.; Hernandez, F. R.; Su, Y.; Zhuang, X.; Zhang, F.; Seifert, G.; Feng, X. Molybdenum Carbide-Embedded Nitrogen-Doped Porous Carbon Nanosheets as Electrocatalysts for Water Splitting in Alkaline Media. *ACS Nano* **2017**, *11*, 3933−3942.

(18) Jing, S.; Zhang, L.; Luo, L.; Lu, J.; Yin, S.; Shen, P. K.; Tsiakaras, P. N-Doped Porous Molybdenum Carbide Nanobelts as Efficient Catalysts for Hydrogen Evolution Reaction. *Appl. Catal. B-Environ.* **2018**, *224*, 533−540.

(19) Yin, Z.; Sun, Y.; Zhu, C.; Li, C.; Zhang, X.; Chen, Y. Bimetallic Ni-Mo Nitride Nanotubes as Highly Active and Stable Bifunctional Electrocatalysts for Full Water Splitting. *J. Mater. Chem. A* **2017**, *5*, 13648−13658.

(20) Xia, C.; Liang, H.; Zhu, J.; Schwingenschlögl, U.; Alshareef, H. N. Active Edge Sites Engineering in Nickel Cobalt Selenide Solid Solutions for Highly Efficient Hydrogen Evolution. *Adv. Energy Mater.* **2017**, *7*, 1602089.

(21) Li, H.; Wen, P.; Li, Q.; Dun, C.; Xing, J.; Lu, C.; Adhikari, S.; Jiang, L.; Carroll, D. L.; Geyer, S. M. Earth-Abundant Iron Diboride (FeB_2) Nanoparticles as Highly Active Bifunctional Electrocatalysts for Overall Water Splitting. *Adv. Energy Mater.* **2017**, *7*,

1700513.

(22) Yin, H.; Zhao, S.; Zhao, K.; Muqsit, A.; Tang, H.; Chang, L.; Zhao, H.; Gao, Y.; Tang, Z. Ultrathin Platinum Nanowires Grown on Single-Layered Nickel Hydroxide with High Hydrogen Evolution Activity. *Nat. Commun.* **2015**, *6*, 6430.

(23) Chen, J.; Yang, Y.; Su, J.; Jiang, P.; Xia, G.; Chen, Q. Enhanced activity for Hydrogen Evolution Reaction over CoFe Catalysts by Alloying with small amount of Pt. *ACS Appl. Mater. Interfaces* **2017**, *9*, 3596−3601.

(24) Cheng, N.; Stambula, S.; Wang, D.; Banis, M. N.; Liu, J.; Riese, A.; Xiao, B.; Li, R.; Sham, T. K.; Liu, L. M.; Botton, G. A.; Sun, X. Platinum Single-Atom and Cluster Catalysis of the Hydrogen Evolution Reaction. *Nat. Commun.* **2016**, *7*, 13638.

(25) Chao, T.; Luo, X.; Chen, W.; Jiang, B.; Ge, J.; Lin, Y.; Wu, G.; Wang, X.; Hu, Y.; Zhuang, Z.; Wu, Y.; Hong, X.; Li, Y. Atomically Dispersed Copper-Platinum Dual Sites Alloyed with Palladium Nanorings Catalyze the Hydrogen Evolution Reaction. *Angew. Chem., Int. Ed.* **2017**, *56*, 16047−16051.

(26) Zhang, H.; An, P.; Zhou, W.; B. Guan, Y.; Zhang, P.; Dong, J.; Lou, X. W. Dynamic Traction of Lattice-Confined Platinum Atoms into Mesoporous Carbon Matrix for Hydrogen Evolution Reaction. *Sci. Adv.* **2018**, *4*, eaao6657.

(27) Zhang, L.; Han, L.; Liu, H.; Liu, X.; Luo, J. Potential-Cycling Synthesis of Single Platinum Atoms for Efficient Hydrogen Evolution in Neutral Media. *Angew. Chem., Int. Ed.* **2017**, *56*, 13694−13698.